



Article

# Effect of Graphene Nanofibers on the Morphological, Structural, Thermal, Phase Transitions and Mechanical Characteristics in Metallocene iPP Based Nanocomposites

Sandra Novo <sup>1,2</sup>, Carmen Fonseca <sup>2</sup>, Rosario Benavente <sup>1</sup>, Enrique Blázquez-Blázquez <sup>1</sup> , María L. Cerrada <sup>1,\*</sup>   
and Ernesto Pérez <sup>1,\*</sup>

<sup>1</sup> Instituto de Ciencia y Tecnología de Polímeros (ICTP-CSIC), Juan de la Cierva 3, 28006 Madrid, Spain; novosandra93@gmail.com (S.N.); rbenavente@ictp.csic.es (R.B.); enrique.blazquez@ictp.csic.es (E.B.-B.)

<sup>2</sup> Mechanical Engineering, Chemistry and Industrial Design Department, Escuela Técnica Superior de Ingeniería y Diseño Industrial, Universidad Politécnica de Madrid (ETSIDI-UPM), Ronda de Valencia 3, 28012 Madrid, Spain; carmen.fonseca@upm.es

\* Correspondence: mlcerrada@ictp.csic.es (M.L.C.); ernestop@ictp.csic.es (E.P.); Tel.: +34-91-258-7474 (M.L.C.)

**Abstract:** Several nanocomposites were prepared by extrusion from a commercial metallocene-type isotactic polypropylene (iPP) and different amounts of two types of graphene (G) nanofibers: ones with a high specific surface, named GHS, and the others with a low specific surface, labeled as GLS. The number of graphene layers was found to be around eight for GLS and about five in the GHS. Scanning electron microscopy (SEM) images of the resultant iPP nanocomposites showed a better homogeneity in the dispersion of the GLS nanofibers within the polymeric matrix compared with the distribution observed for the GHS ones. Crystallinity in the nanocomposites turned out to be dependent upon graphene content and upon thermal treatment applied during film preparation, the effect of the nature of the nanofiber being negligible. Graphene exerted a noticeable nucleating effect in the iPP crystallization. Furthermore, thermal stability was enlarged, shifting to higher temperatures, with increasing nanofiber amount. The mechanical response changed significantly with nanofiber type, along with its content, together with the thermal treatment applied to the nanocomposites. Features of nanofiber surface played a key role in the ultimate properties related to superficial and bulk stiffness.

**Keywords:** metallocene iPP; graphene nanofibers; nanocomposites; crystalline lattice; nucleating effect; phase transitions; thermal stability; mechanical properties



**Citation:** Novo, S.; Fonseca, C.; Benavente, R.; Blázquez-Blázquez, E.; Cerrada, M.L.; Pérez, E. Effect of Graphene Nanofibers on the Morphological, Structural, Thermal, Phase Transitions and Mechanical Characteristics in Metallocene iPP Based Nanocomposites. *J. Compos. Sci.* **2022**, *6*, 161. <https://doi.org/10.3390/jcs6060161>

Academic Editors: Thanasis Triantafyllou and Costas Charitidis

Received: 26 April 2022

Accepted: 30 May 2022

Published: 1 June 2022

**Publisher's Note:** MDPI stays neutral with regard to jurisdictional claims in published maps and institutional affiliations.



**Copyright:** © 2022 by the authors. Licensee MDPI, Basel, Switzerland. This article is an open access article distributed under the terms and conditions of the Creative Commons Attribution (CC BY) license (<https://creativecommons.org/licenses/by/4.0/>).

## 1. Introduction

Industrial interest in polypropylene, PP, especially under its isotactic configuration, iPP, is clearly evident by the fact that iPP is one of the polyolefins with higher commercial use in multiple applications. This extensive applicability is due to its ease of processing, good heat resistance, excellent mechanical properties, and low cost. Its poor impact resistance at low temperatures can be considered one of its major shortcomings. Accordingly, research on iPP is ongoing, looking for optimization and design of new applications [1]. Changes in its structure can be triggered by several approaches: (a) the synthetic protocol, varying types of the catalyst used (conventional or latest generation Ziegler Natta (ZN) catalysts [1,2] as well as the so-called metallocenes ones [1,3,4] that allow copolymerization with other  $\alpha$ -olefins for manufacturing random or block copolymers, among other possibilities); (b) blending with other polyolefins, such as polyethylene, PE, or ethylene copolymers with  $\alpha$ -olefins as counits [5–7]. Incorporation of additives for modifying crystallization rate in order to optimize transparency, and for controlling the type of crystalline polymorph developed [8,9]. Furthermore, fillers are sometimes added to decrease the final price or to promote certain

functionalities, such as permeability to gases [10,11], antimicrobial characteristics [12], electromagnetic interference features [13], or mechanical reinforcement [14,15].

The development of metallocene iPPs has not stopped since their discovery in the 1990s. They can be synthesized either under homogenous or heterogeneous conditions [16,17]. Enhanced impact strength is exhibited in these metallocene iPPs compared with this property shown by iPP synthesized with ZN catalysts, being probably associated with the smaller size of the crystallites developed in the former [7,8].

In parallel, applications of graphene (G) continue growing at present, seeking new unexplored fields. Much work has been focused on the preparation of nanocomposites based on graphene or its derivatives with numerous polymeric matrices. These graphene derivatives incorporated to iPP (mainly the ones obtained with ZN catalysts) were basically referred to as modified graphene, graphene oxide (GO), or graphene (nano)fibers [18,19].

Graphene nanoplatelets (GNP) were also selected as alternative reinforcing fillers to enhance the properties of iPP. Different compatibilizer agents were used, mainly polypropylene grafted maleic anhydride (PP-g-MA) and ethylene-octene elastomer grafted maleic anhydride (POE-g-MA) [20] in order to trigger interactions at interfaces of these two components, iPP and GNP.

Crystallization temperature ( $T_c$ ) of iPP was found to be shifted up to 10 °C in nanocomposites achieved by in situ polymerization of propylene in presence of graphene nanosheet (GNS) compared with that observed in the neat iPP [21,22]. Changes in properties (thermal stability, mechanical properties, and electrical characteristics) were even more noticeable if nanocomposites were prepared by in situ polymerization from copolymers of propylene with  $\alpha$ -olefins and GNS [23,24].

The aim of this research is focused on the obtainment of iPP nanocomposites with graphene nanofibers using the extrusion as a preparation strategy, since this methodology is from an industrial standpoint, more versatile and attractive than in situ polymerization. Therefore, several contents of two types of graphene nanofibers with different specific surfaces have been incorporated into a commercial metallocene-type iPP matrix. An exhaustive characterization has been carried out in order to elucidate the importance of that type of nanofiber, its content, and the thermal history applied during processing exerted on films obtained from the resultant nanocomposites. A metallocene iPP has been selected as matrix because there are scarce investigations in literature concerning these nanocomposites, especially when processed by melt extrusion.

## 2. Materials and Methods

### 2.1. Materials

An isotactic metallocene iPP, with trademark HM562P ( $MFI = 15$  g/10 min according to standard ISO 1133 at 210 °C, 2.16 kg) and kindly supplied by Basell (Rotterdam, The Netherlands), was used. It is named from now as HMP.

Two types of graphene nanofibers, kindly supplied by Graphenano (Yecla, Murcia), with different specific surfaces, were employed. On one hand, graphene nanofibers with high specific surface, the so-called GHS, shows the following characteristics: high specific surface, which ranged from 300 to 400 m<sup>2</sup>/g; fiber diameter of 5–160 nm; fiber length > 20 nm; density at 20 °C = 0.4–0.6 g/cm<sup>3</sup>. On the other hand, graphene nanofibers with low specific surface, identified as GLS, exhibit a specific surface from 70 to 250 m<sup>2</sup>/g; fiber diameter of 5–160 nm; fiber length > 20 nm; density at 20 °C = 0.2–0.3 g/cm<sup>3</sup>.

### 2.2. Extrusion of the Nanocomposites

HMP pellets were crio-milled in liquid nitrogen, before extrusion, using a SCHOTI grinder (Schott Maschinenbau, Kupferberg, Germany), working at a frequency of 20,000 min<sup>-1</sup> in order to reduce the pellet size and promote a better dispersion of the graphene nanofibers into this HMP matrix. Graphene fibers were first dispersed in toluene using ultrasounds before blending with the iPP.

Nanocomposites containing a weight percentage (wt.%) of 0.1, 0.2, 0.5, 1.0, 5.0, and 10.0 in each kind of graphene nanofibers were then prepared by melt extrusion in a Rondol Microlab Twin Screw mini-extruder (Rondol Industrie, Nancy, France), employing 10 mm diameter extrusion screws, working at 60 rpm and using 115 °C/170 °C/180 °C/185 °C/190 °C as temperature profile. The different nanocomposites were labeled as HMP $x$ GHS or HMP $x$ GLS, where  $x$  refers to the wt.% content in nanofibers and GHS or GLS corresponds to the type of graphene nanofiber incorporated.

### 2.3. Preparation of the Films

Films of these HMP nanocomposites with different contents in GHS or GLS nanofibers were obtained by compression molding in a Collin press (Collin GmbH, Maitenbeth, Germany) between hot plates (210 °C) at a pressure of 20 bar for 3 min. In the subsequent cooling from the melt, two different thermal histories were applied by variation of cooling rate: 80 °C/min (specimens named Q) and 2 °C/min (designated as S samples). Thickness of the films was around 300  $\mu$ m.

### 2.4. Characterization Techniques

A Philips XL30 ESEM equipment (Philips, Eindhoven, The Netherlands) was used for the morphological details of the different materials, working at an acceleration voltage of 15 kV. Samples were metallized with an 80:20 gold/palladium (Au/Pd) alloy in order to obtain a better image resolution.

Raman spectra were recorded in a Renishaw InVia Reflex Raman system (Renishaw plc, Wotton-under-Edge, UK), using an Ar-Kr laser with a wavelength of 514 nm, and a resolution of 1.7  $\mu$ m, with a charge-coupled device (CCD) detector. The measurements were taken by incidence of laser on the samples with a power of 10%, accumulating 10 scans and with an exposure time of 10 s.

X-ray diffraction, XRD, measurements were performed at room temperature using a Bruker D8 Advance diffractometer (Bruker, Madison, WI, USA), with CuK $\alpha$  radiation ( $\lambda = 0.1542$  nm), in the angular  $2\theta$  interval between 5° and 35°. Graphene nanofibers were fine powders and, then, the X-ray diffractograms of the neat nanofibers were obtained by wrapping them in aluminum (Al) foil, in order to avoid equipment contamination. The number of graphene layers was assessed by the Scherrer equation [25], considering the 002 direction (diffraction peak centered at  $2\theta = 26.6^\circ$ ):

$$l_c^{(002)} = \frac{k \cdot \lambda}{\beta_0 \cdot \cos \theta} \quad (1)$$

where  $k = 0.88$ ,  $\lambda = 0.1542$  nm and  $\beta_0$  is the width of the peak at half height.

Crystallinity ( $f_c$ ) estimation by XRD was performed in the nanocomposites by subtraction of the corresponding amorphous iPP halo, using for that the totally amorphous profile of an elastomeric PP sample [26,27].

Calorimetric analyses by differential scanning calorimetry (DSC) were carried out in a TA Instruments TA-Q100 calorimeter (TA Instruments, New Castle, DE, USA) connected to a cooling system and calibrated with different standards. The sample weights ranged from 7 to 10 mg. The heating and cooling rates used were 20 °C/min. For crystallinity ( $f_c$ ) determination, a value of 165 J/g has been considered as the enthalpy of fusion for a perfectly crystalline iPP material [9,28,29]. The enthalpy deduced from the melting curves in the nanocomposites has been previously normalized to the actual polymer content in the sample before crystallinity estimation.

A TA Instruments TA-Q500 equipment (TA Instruments, New Castle, DE, USA) was used for thermogravimetric analyses under a nitrogen (N $_2$ ) atmosphere in a temperature range between 30 to 800 °C. Heating rate used was 10 °C/min.

A Vickers indenter attached to a Leitz microhardness (MH) tester (Leitz GmbH, Oberkochen, Germany) was used to carry out microindentation measurements. Experi-

ments were undertaken at 25 °C. A contact load of 0.98 N and a contact time of 25 s were employed. *MH* values (in MPa) were calculated according to the relationship [30,31]:

$$MH = 2\sin 68^\circ \left( \frac{P}{d^2} \right) \quad (2)$$

where *P* (in N) is the contact load and *d* (in mm) is the diagonal length of the projected indentation area.

Stress-strain curves were achieved at room temperature employing a DX2000 QTest Elite MTS dynamometer (MTS Systems, Eden Prairie, MN, USA), working at a stretching rate of 10 mm/min. Dumbbell-shaped specimens with gauge dimension of 15 mm in length and 2 mm in width were punched out from the compression molded sheets with a standardized die. Thickness of the specimens was around 0.3 mm. Different mechanical parameters were calculated from these stress-strain curves. At least five specimens were tested for each material, and the standard deviation of mean values was found to be less than 8%.

### 3. Results

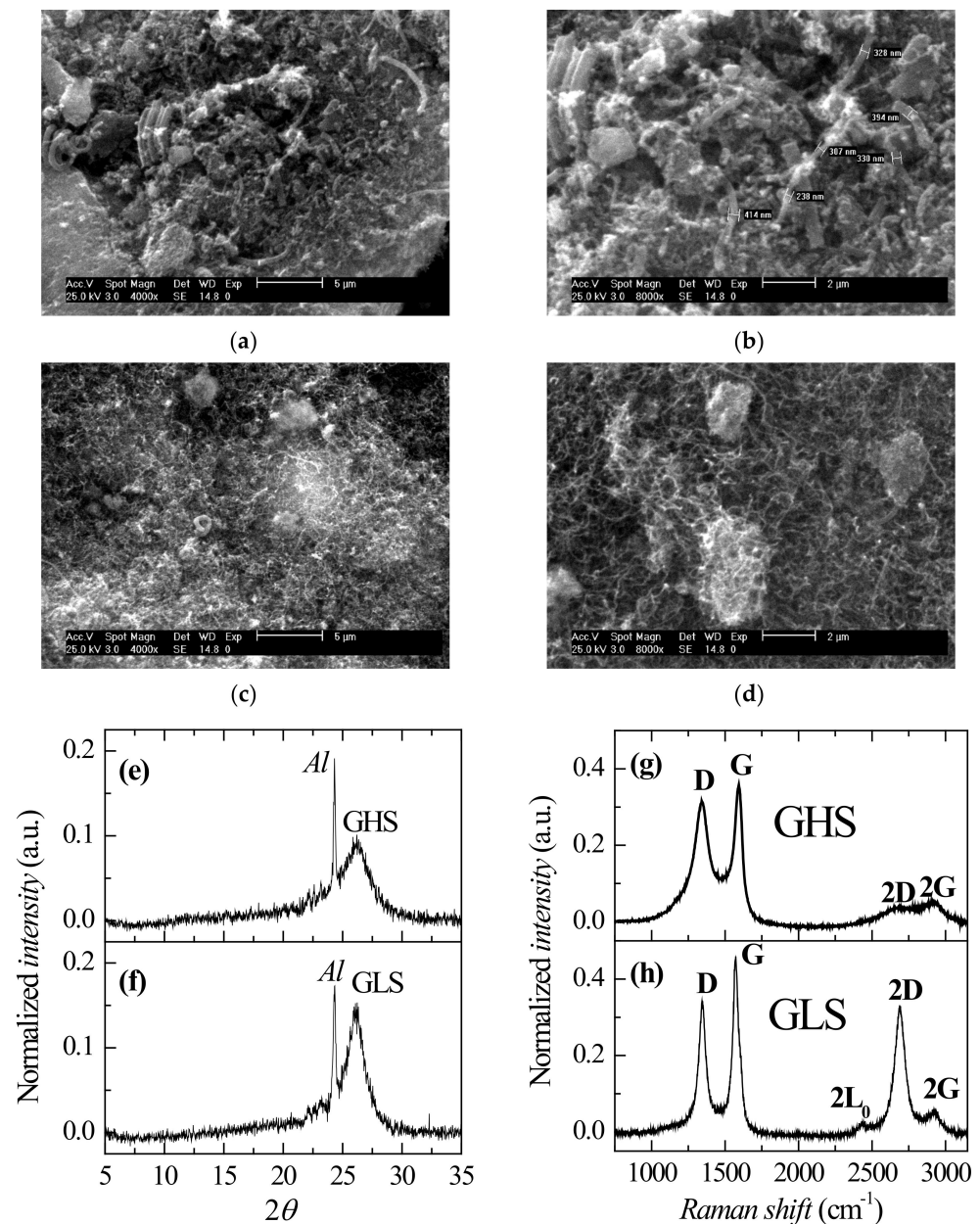
#### 3.1. Characterization of Graphene Nanofibers

Figure 1 shows the main characteristics exhibited by the two types of graphene nanofibers used, determined through different techniques: SEM, X-ray diffraction, and Raman spectroscopy. SEM images (Figure 1a,b for GHS and Figure 1c,d for GLS) show a better homogeneity in the case of GLS nanofibers with respect to the GHS ones, which is attributed to the higher specific surface of the latest. This greater surface could promote a large agglomeration, tending toward reverting the graphitic configuration by means of  $\pi$ - $\pi$  bonds and remaining Van der Waals interaction forces in the nanofibers.

Figure 1e,f display the X-ray diffractograms for these GHS and GLS nanofibers. These experiments were performed by wrapping these nanofibers within Al foil, so that the narrow diffraction peak appearing at around 24.3° corresponds to Al, which is located next to the wide 002 diffraction of the expanded graphene that is placed at about 26.2°. The number of graphene layers can be estimated by the Scherrer equation from that diffraction peak. A peak width at half height of 2.45° for  $\beta_0$  in Equation (1) was obtained for the GHS nanofibers. According to the Scherrer equation, the number of layers is deduced by dividing the determined lamella size, 34.8 Å, by the theoretical separation among graphene layers, similarly to the reported procedure [32]. Thus, the resulting number of layers in GHS is 5.1. The diffraction found for GLS nanofibers is noticeably narrower and a peak width at half height of 1.62° for  $\beta_0$  was deduced, leading to a lamella size of 55.6 Å. Accordingly, the number of graphene layers for GLS is equal to 8.1.

Raman spectroscopy provides a lot of information about graphite and its derivatives. The spectrum of pure graphite without impurities only presents a narrow and intense band located at approximately 1580 cm<sup>-1</sup> [33,34]. This band is known as the G band and is related to the structural order of graphite, and is due to the relative movement of the carbon atoms linked by sp<sup>2</sup> bonding along the bond direction. When the graphite moves away from its state of purity, due to the existence of specific defects, its structural order is lost, and a new band appears in the first-order region of the spectrum (band D at 1340 cm<sup>-1</sup>) [35]. The second-order region is located in the 2300–3300 cm<sup>-1</sup> range, and overtones of the first-order bands appear also in that range. The most characteristic band in this zone is found at about 2700 cm<sup>-1</sup>, and is known as 2D because this is the D-band overtone. As the graphite moves away from its ideal structure, the second-order bands are widened and their intensity is reduced, until they overlap each other, making it impossible to identify them individually. Raman spectra corresponding to pure graphene show, therefore, some differences from those appearing in graphite. The most prominent band is the 2D one, which is very narrow and intense [36,37], being very sensitive to the number of graphene layers [33].





**Figure 1.** SEM micrographs of graphene nanofibers at two magnifications: GHS (a,b) and GLS (c,d). X-ray diffractograms of GHS (e) and GLS (f) nanofibers. These nanofibers were wrapped in aluminum foil (see Al diffraction peak at a value of  $2\theta$  of  $24.3^\circ$ ). Raman spectra of GHS (g) and GLS (h) graphene nanofibers.

Figure 1g,h show the Raman spectra for the neat GHS and GLS nanofibers. The former exhibits two very intense bands at the positions of  $1340$  and  $1593\text{ cm}^{-1}$ , which correspond to the D and G bands [33,34], respectively. In the second-order interval, two low-intensity peaks are observed, one appearing at  $2675\text{ cm}^{-1}$  and the other band at  $2920\text{ cm}^{-1}$ , which are ascribed to the 2D and 2G bands, that in turn are associated with the overtones of the bands D and G, respectively. Regarding the spectrum of GLS nanofibers represented in Figure 1h, the D and G bands also appear at a location of  $1346$  and  $1570\text{ cm}^{-1}$ , respectively. In the second-order region, a very intense peak is observed at  $2686\text{ cm}^{-1}$ , which corresponds to the 2D band, as well as a peak at  $2923\text{ cm}^{-1}$  that is associated with the overtone of the G band of the first-order spectrum. In this case, the presence of an additional peak at  $2430\text{ cm}^{-1}$  is also noted, which is ascribed to the  $2L_0$  band. The appearance of the second-order zone boundary phonon (2D) peak at  $2440\text{ cm}^{-1}$  together with the shoulder

peak at  $2930\text{ cm}^{-1}$ , which is also observed in sonicated samples [35], are usually indicative of specimens constituted by few layers of graphene.

Therefore, an evident change is deduced from these two spectra seen in Figure 1g,h for the second-order interval of both types of graphene nanofibers. The 2D band for GLS is a very intense and narrow peak associated with expanded graphene. In contrast, that band is wide and appears with low intensity in GHS, showing a profile more similar to the graphite spectrum [32]. These characteristics point out that a number of layers in GHS and GLS are noticeably different, as already deduced from the XRD results.

Band D is attributed to the presence of defects and curvatures in the graphene and in carbonaceous structures, while band G is associated with ordered arrangements. The fact that band D appears in both types of graphene nanofibers indicates that these two structures have defects or impurities. In fact, an increase in the ratio between the areas of the D and G bands,  $I^D/I^G$ , is generally indicative of a growing number of defects, so that a value as low as 0.2 was found [38] for graphite while a much higher ratio of 1.54 was attained for graphene. The values of  $I^D/I^G$  deduced from Figure 1g,h are 1.6 and 1.0 for GHS and GLS, respectively, thus pointing out again the substantial differences between GHS and GLS nanofibers.

### 3.2. Morphological Characterization of Nanocomposites

The top pictures in Figure 2 show images for the HMP homopolymer and the nanocomposites with 5 wt.% of GHS and GLS nanofibers at a  $1000\times$  magnification after cryogenic fracture in liquid nitrogen and coated with a thin Au layer. Significant morphological differences are noticed, displaying a smooth surface for HMP, which is characteristic of ductile behavior, while a more fragile fracture is seen in the nanocomposites.

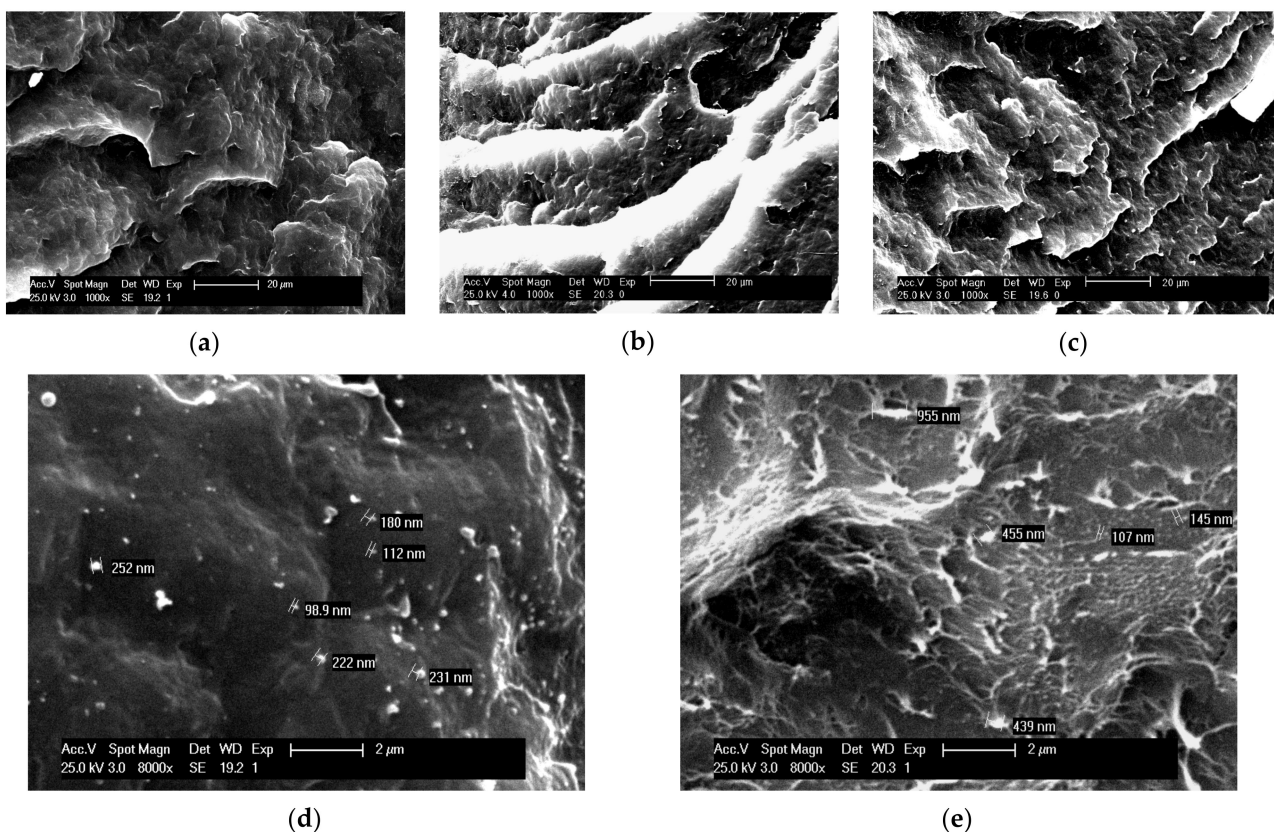


**Figure 2.** SEM images at a magnification of  $1000\times$  for: (a) HMP; (b) HMP5GHS; and, (c) HMP5GLS. SEM images at a magnification of  $8000\times$  for: (d) HMP5GLS and (e) HMP10GLS.

The HMP5GLS material, containing GLS nanofibers, shows a failure with a laminar-like surface in contrast to the one observed in the HMP5GHS nanocomposite. The GHS hybrids seem to display a weaker failure, fact that is associated with the intrinsic higher specific surface of the nanofibers that hinders a more intimate contact with the PP matrix.

Fiber size and dispersion within the polymer are better evaluated from SEM images at higher magnifications (see bottom pictures in Figure 2), where graphene is displayed as the bright points observed in the different images. Fibers in the transverse direction are also noticeable, mainly at the highest GLS composition, some of them being agglomerated. Their average width is about 250 nm, which is in agreement with the manufacturer's specification. A comparison of these results with those attained by Acahby et al. [39] indicates a reasonably uniform graphene dispersion, aggregates being also evident in PP nanocomposites with a 2 wt.% graphene nanosheets. Bian et al. [40] observed a smooth surface by SEM for the hybrids based on PP with graphene/SiO<sub>2</sub>. SEM images for nanocomposites of polypropylene with an amine modified GO revealed [41] that neat GO was aggregated partially when it was embedded in the PP matrix while a better dispersion was achieved by its modification with the amine. Analogous results were also shown in PP nanocomposites with reduced graphene, whose surface was coated with a polymer film [38]. An agglomeration increase was reported [42] in GO/short carbon fiber (SCF)/polypropylene (PP) composites, from 0.5 wt.% to 1 wt.% in GO fraction. Accordingly, pictures for the PP nanocomposites here analyzed point out a rather good homogeneity, especially taking into account that neither compatibilizer nor modification of graphene nanofibers was used.

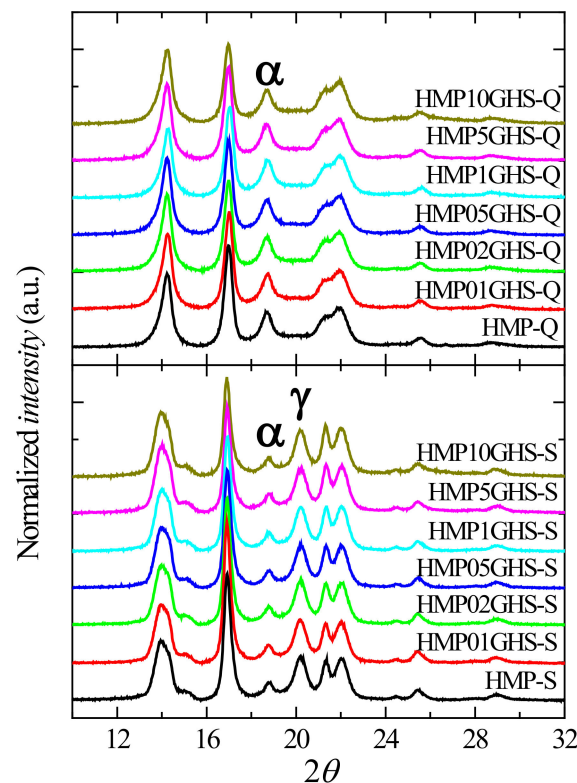
### 3.3. Structural Evaluation of Nanocomposites

Figure 3 shows the pure crystalline profiles in different nanocomposites, after subtracting the amorphous halo (see Section 2.4.), for the two thermal treatments applied, Q and S. The corresponding values of crystallinity are listed in Table 1. For Q samples, the crystalline reflections that appear in the diffractograms at 14.1°, 16.9°, 18.5°, 21.1°, 21.8°, and 25.8° [43,44], as seen in the upper plot of Figure 3, are those characteristic of the monoclinic  $\alpha$  form. The S samples additionally display a clear diffraction located at 20.3°, which is characteristic of the orthorhombic  $\gamma$  modification. This polymorph has been triggered by the slow cooling applied during the compression molding. This  $\gamma$  lattice is not the only crystalline structure existing in these slowly crystallized specimens but a significant proportion of monoclinic  $\alpha$  form is also present (see below). The diffraction corresponding to the graphene is barely observed as a shoulder, being centered at 26.2°, in the nanocomposites with the highest contents since it is partially overlapped with the diffraction at 25.5° corresponding to the iPP.

Table 1 shows the degree of crystallinity obtained by X-ray diffraction ( $f_c^{XRD}$ ) for all of the GHS and GLS nanocomposites under the two thermal treatments, Q and S. According to these results, higher  $f_c^{XRD}$  values are achieved in the S samples in comparison with those found in the Q ones, as expected. Moreover, there is a small but appreciable increase in crystallinity in all cases as the graphene content increases.

As commented above, S samples exhibit the coexistence of two crystalline forms,  $\alpha$ , and  $\gamma$ . The polymorphic behavior of iPP has been widely described, exhibiting three main crystalline forms, named as  $\alpha$ ,  $\beta$ , and  $\gamma$  [45,46]. The more stable modification is the  $\alpha$  monoclinic lattice, but a slow rate of cooling promotes the formation of the  $\gamma$  orthorhombic form in metallocene iPPs (and in other copolymers). The  $\beta$  polymorph usually appears by the addition of specific additives. Another phase of intermediate order is the mesomorphic form, generally obtained by fast quenching [47,48]. Furthermore, a new polymorph, the trigonal  $\delta$  modification, has been described in propylene copolymers with relatively large contents in 1-pentene or 1-hexene [49–51] and also in terpolymers with both counits [52] or with 1-pentene and 1-heptene used as comonomers [53]. Relative contents of the  $\alpha$  and  $\gamma$  modifications, shown also in Table 1, for the nanocomposites subjected to a thermal treatment S, i.e., those films achieved by a slow cooling from the melt, have been determined as described earlier [54].





**Figure 3.** X-ray diffractograms, after subtraction of the amorphous component, for the different nanocomposites with GHS nanofibers under Q and S thermal treatments.

**Table 1.** Degree of crystallinity ( $f_c^{XRD}$ ) (%) determined by X-ray diffraction for all the different nanocomposites under the Q and S thermal treatments. Proportion in  $\alpha$  and  $\gamma$  forms in the S specimens where these two polymorphs coexist.

Sample	$f_c^{XRD}$ (%)		Polymorphs Content in the S Specimens	
	Q	S	$\alpha$ (%)	$\gamma$ (%)
HMP	58	62	15	47
HMP01GHS	59	63	13	50
HMP02GHS	60	64	13	51
HMP05GHS	61	65	14	51
HMP1GHS	61	65	13	52
HMP5GHS	62	66	11	55
HMP10GHS	62	67	11	56
HMP01GLS	59	64	14	50
HMP02GLS	59	66	12	54
HMP05GLS	60	66	11	55
HMP1GLS	61	67	11	56
HMP5GLS	61	68	14	54
HMP10GLS	62	69	13	56

As can be deduced from the crystalline profiles in Figure 3 and the results listed in the two latest columns of Table 1, the major crystalline polymorph is the  $\gamma$  phase in the slowly crystallized nanocomposites. Moreover, the presence of graphene favors the obtainment of this  $\gamma$  form, increasing its fraction as the graphene content rises in the nanocomposite, independently of the type of nanofiber used. This favorable formation of the  $\gamma$  modification was analogously observed when graphene nanosheets were employed [24] instead of the graphene nanofibers used in the present materials.



Developments of small amounts of the  $\beta$  modification were also described in iPP nanocomposites with graphene. In this context, contradictory behaviors were reported: a research showed that the  $\beta$  form was only seen in the neat iPP, disappearing in the nanocomposites [32], while opposite features were described in other studies [34,55], such as the  $\beta$  form being not observed in the pristine polymer and was noticeable at very small amounts in the nanocomposites. To understand these facts, it is important to consider that, firstly, rather low contents of  $\beta$  form were involved; and, secondly, those investigations were dealing with iPP synthesized with conventional Ziegler-Natta catalysts, while iPP in the present study was synthesized with a metallocene system. A close inspection of Figure 3 allows concluding that the  $\beta$  modification is not attained in these present materials. Another research with graphene platelets [56] found only the sharp diffractions corresponding to the  $\alpha$  form for both neat iPP and graphene nanocomposite films, and the patterns of the nanocomposites were almost identical to that exhibited by the neat polymer, indicating that graphene platelets do not affect the crystalline characteristics in the nanocomposites.

Concerning structural information from Raman spectroscopy, Figure 4 displays the spectra for the pristine HMP and the different HMP $\alpha$ GHS nanocomposites. The more important bands associated with PP are those appearing at 810 and 843  $\text{cm}^{-1}$ , related to its isotacticity and to the degree of crystallinity. Bands at 976, 1154, and 1448  $\text{cm}^{-1}$  are not specific of an ordered conformation and are mainly due to the vibrational location within the chain segments.

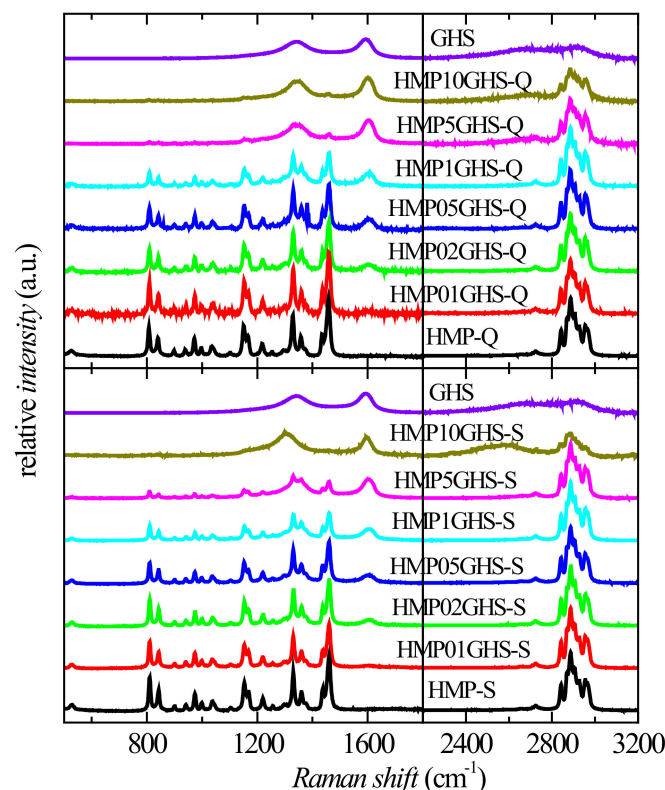


**Figure 4.** Raman spectra for the HMP $\alpha$ GHS nanocomposites under the Q and S thermal treatments.

Furthermore, Figure 4 shows a remarkable change between spectra from the neat iPP and the nanocomposites with low nanofibers contents and those hybrids at graphene incorporation higher than 1 wt.%, spectrum being practically dominated by nanofibers in nanocomposites with a content above 5 wt.%. Since most of their bands are superimposed on the ones from iPP, obtainment of valuable information is not possible. The characteristic G band of graphene at around 1600  $\text{cm}^{-1}$  is the only one that does not overlap with iPP and its intensity increases rather proportionally with graphene content. Rather similar spectra

are achieved for all of the nanocomposites, independently of incorporation of the GLS or GHS nanofibers.

### 3.4. Thermal Stability and Phase Transitions

Figure 5 shows the thermogravimetric, TGA, curves for the different nanocomposites performed under an inert environment. A single degradation stage (either in the weight loss or the derivatives curves) is noticed in all of them, independently of the nanofiber content and on the type of nanofiber incorporated. The existence of a unique process is commonly found in iPP under these conditions. Nevertheless, its location is moved to higher temperatures by the presence of graphene and thus thermal stability is increased as the nanofiber content in the nanocomposites rises, although not in a linear way. In fact, the incorporation of a very low amount of graphene, independently of being GHS or GLS, moves the maximum degradation temperature up to 20 °C. Thus, this temperature appears at 450 °C in the pristine HMP homopolymer and at around 470 °C for HMP01GHS and for HMP01GLS specimens while the HMP10GHS and HMP10GLS samples exhibit the maximum peak at 480 °C. There is not an appreciable difference in the thermal stability of the nanocomposites that incorporate these two types of nanofibers. A superior thermal stability was also described in nanocomposites based on PP and GO functionalized with SiO<sub>2</sub> [40] compared to the one exhibited by the neat PP, similar to what is found in these two families of HMP materials.

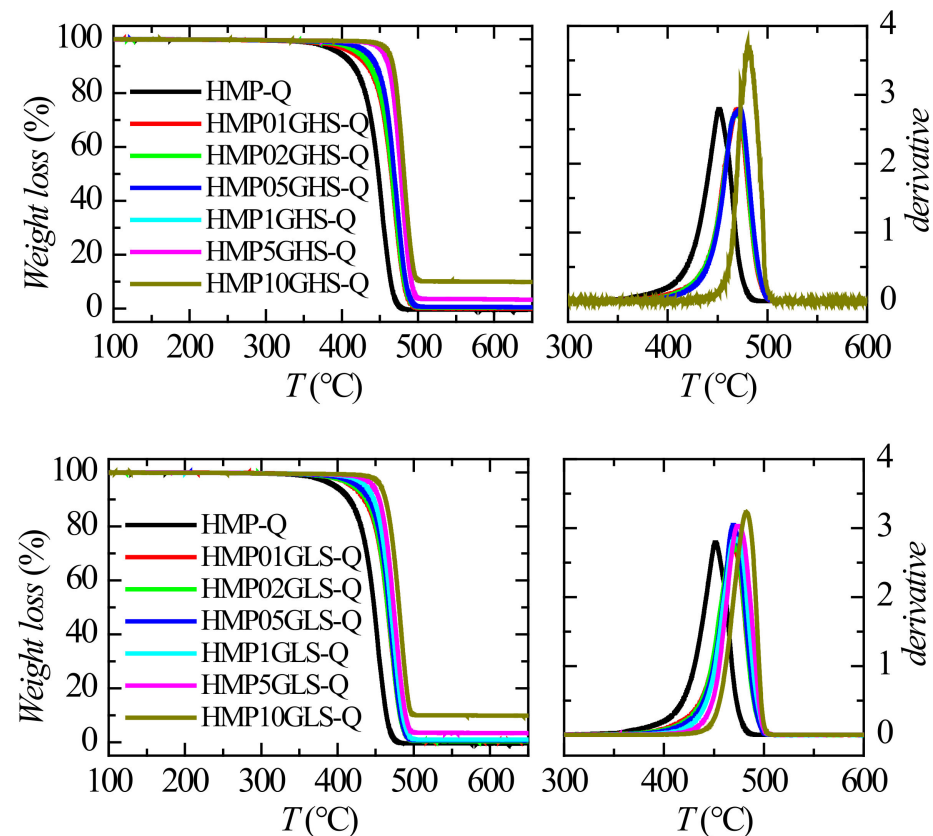


**Figure 5.** Weight loss curves (left) and their derivatives (right) as a function of temperature for the different nanocomposites with the Q thermal treatment.

Once the HMP matrix finishes its degradation at about 500 °C, the remaining mass at higher temperatures is related, as observed in Figure 5, to the graphene nanofiber content for each nanocomposite.

Figure 6 shows the DSC first melting curves for the different GHS films obtained under the two thermal treatments, Q and S. Melting curves for the GLS nanocomposites, not shown, are rather similar. Table 2 collects the results for the location of the distinct

transitions (glass transition, melting, and crystallization) for all of the specimens. At a given set of materials, those prepared using the GHS or GLS nanofibers, evident differences are exhibited depending on the thermal treatment applied. The S samples show a noticeable bimodal melting behavior ascribed, on one hand, to the fusion of the coexistent  $\gamma$  and  $\alpha$  crystalline forms and, on the other hand, to the fact that the  $\gamma$  polymorph is found in the majority, as previously confirmed from X-ray diffraction patterns, showing its melting temperature at about 142 °C. The  $\alpha$  polymorph melts at slightly higher temperatures. Furthermore, the crystallinity estimated by DSC ( $f_c^{\text{DSC}}$ ) (see values in Table 2) in these S samples is considerably higher than those attained for the Q specimens. This observation is in agreement with the results obtained from X-ray diffraction (see Table 1). At a specific thermal treatment,  $f_c^{\text{DSC}}$  is raised as increasing graphene content in the nanocomposites independently of the nanofiber used. This rise is for the S samples greater than in the Q in these two families.

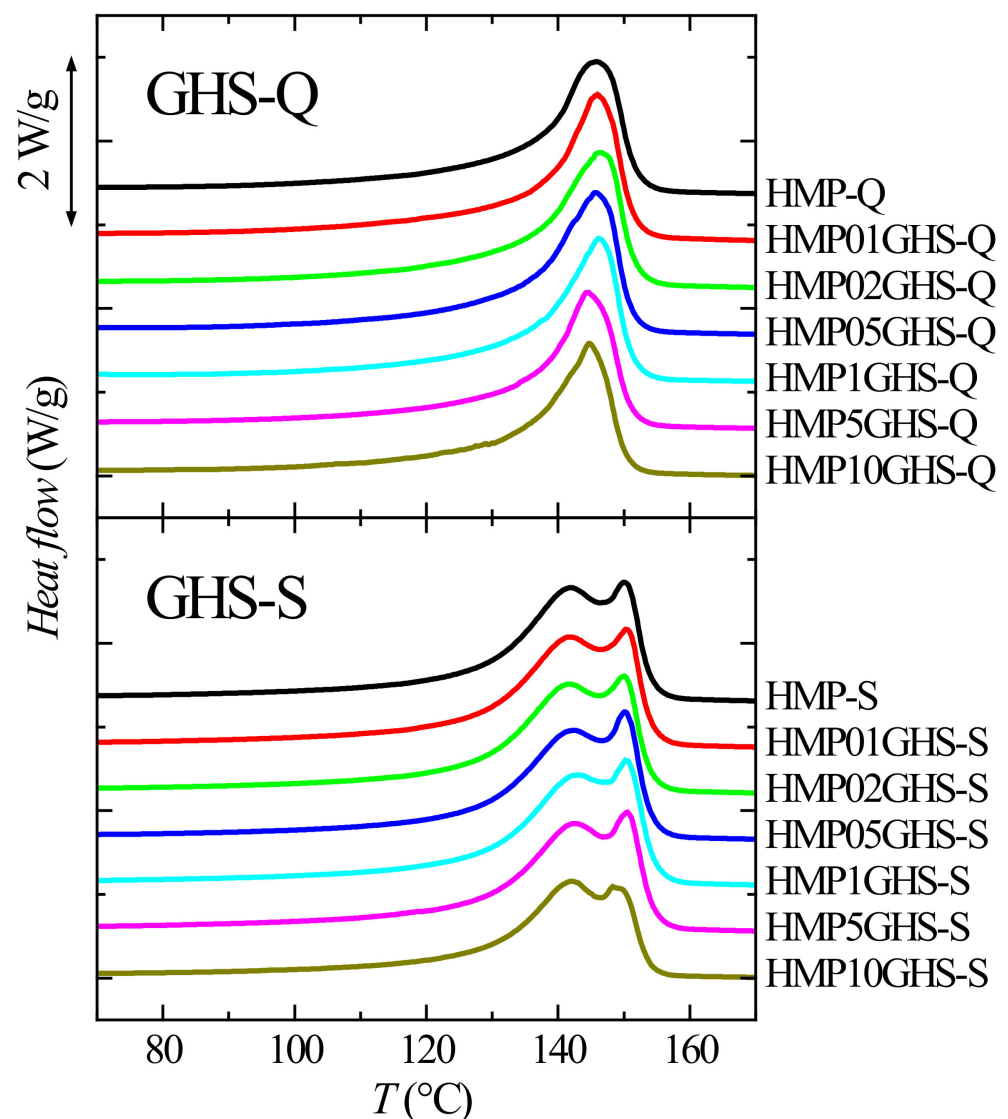


**Figure 6.** DSC first melting curves for the neat HMP and the GHS nanocomposites at the two thermal treatments applied: Q (top plot) and S (bottom plot).

The glass transition (not shown in the temperature interval represented in Figure 6) is shifted to higher temperatures as the nanofiber content increases in these two families of graphene nanocomposites (see Table 2). Moreover, the S samples mostly show slightly higher values of glass transition temperature ( $T_g$ ) than the ones observed in the Q samples.

This fact can be associated with the greater mobility restrictions existing in the former due to the presence of more crystals, i.e., higher crystallinity, whose size is also larger as deduced from the values of the melting temperature ( $T_m$ ). This assumption in the S samples is deduced from the  $T_m$  appearing at the highest temperature, which is the one corresponding to the  $\alpha$  crystallites (that is the only polymorph present in the Q specimens).

**Table 2.** Glass transition temperature ( $T_g$ ), melting temperature ( $T_m$ ), and total DSC crystallinity degree ( $f_c^{DSC}$ ) calculated from the first melting run for the different nanocomposites processed under the two Q and S thermal treatments. Values of crystallization temperature ( $T_c$ ) in the subsequent cooling are also listed.

Sample	$T_g$ (°C)		$T_m$ (°C)			$f_c^{DSC}$ (%)		$T_c$ (°C)
	Q	S	$\alpha^Q$	$\gamma^S$	$\alpha^S$	Q	S	
HMP	−8	−6	146.0	142.0	150.5	58	64	112.0
HMP01GHS	−8	−5	146.5	141.5	150.5	59	65	112.5
HMP02GHS	−6	−5	146.5	142.0	150.5	59	65	113.0
HMP05GHS	−5	−5	147.0	142.0	150.0	59	65	113.5
HMP1GHS	−3	−4	147.0	142.5	150.5	59	65	113.5
HMP5GHS	−3	−3	145.5	142.5	151.0	60	67	113.5
HMP10GHS	−1	−2	145.0	142.5	150.0	60	68	115.0
HMP01GLS	−4	−3	147.0	142.0	150.0	59	65	113.0
HMP02GLS	−3	−2	146.0	142.0	150.5	60	66	114.0
HMP05GLS	−3	−1	147.0	141.0	150.0	60	66	114.0
HMP1GLS	−1	−1	147.0	141.0	150.0	60	67	114.0
HMP5GLS	0	1	145.5	141.5	150.0	61	68	114.5
HMP10GLS	-	-	145.5	141.0	150.5	62	69	114.5

Once the materials are molten, all the samples show on cooling a crystallization process, whose crystallization temperature ( $T_c$ ) is located in the interval ranging from 112 to 115 °C, as listed in Table 2. The presence of nanofibers exerts a nucleating effect on the iPP crystallization and, then, values of  $T_c$  are moved to higher temperatures as graphene content increases. This shift up of  $T_c$  is beneficial from an industrial point of view since it implies shorter cycle times during processing. This nucleation effect has been also observed in other iPPs composites incorporating different types of graphene or derivatives [24,38–41,56,57]. The subsequent second melting curves are rather similar in both shape and  $T_m$  location for all the different samples, independently of the type of nanofiber incorporated, GHS or GLS.

### 3.5. Final Mechanical Properties

Morphological and structural features are key variables for the final mechanical properties exhibited by polymeric materials. In order to evaluate their influence, microhardness ( $MH$ ) and stress-strain behavior under tension have been evaluated.

Microhardness ( $MH$ ) measures the permanent deformation in a material under the action of a constant load at a given time [58,59]. This magnitude is related to the stiffness of the material, so that its value strongly depends on the amorphous and crystalline characteristics of the polymers, including crystallite size or degree of crystallinity, as well as type and content in (nano)fillers [17,31,59] for (nano)composites.

$MH$  values are shown in Figure 7 for these hybrids containing graphene nanofibers. A clear increase is observed as graphene content is enlarged, independently of the kind of nanofiber used. This  $MH$  rise grows up to 30% for the GHS nanocomposites while the increase reaches 46% for the GLS materials in Q specimens. An analogous trend is also noticed in the S samples, as deduced also from Figure 7. Now,  $MH$  values are higher than the ones observed in the Q specimens, indicating the larger stiffness found in the S samples compared with their Q counterparts. This greater rigidity in the S specimens is



associated with their higher degree of crystallinity together with their thicker and more perfect crystallites.

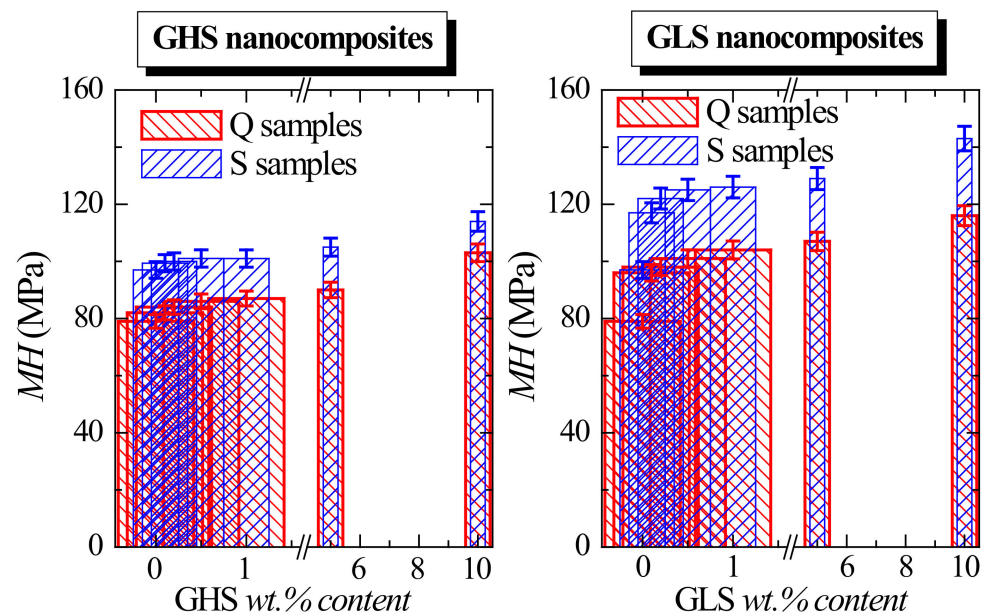


**Figure 7.** Values of  $MH$ , deduced from microhardness tests for the metallocene iPP matrix and nanocomposites with different contents and types of graphene nanofibers.

Furthermore,  $MH$  provides an idea of the homogeneity in the filler distribution, i.e., its magnitude is sensitive to heterogeneities [6]. Therefore, if large and different areas of films are tested at a given material, the quality of nanofiller dispersion could be estimated. Standard deviations derived from these tests are not significant and, consequently, a rather satisfactory distribution of nanofibers is deduced.

It is also remarkable from Figure 7 that  $MH$  values are at a given nanofiber content noticeably larger in the HMP $\times$ GLS nanocomposites than in the HMP $\times$ GHS ones. Details from crystalline regions do not seem to trigger these differences since the degree of crystallinity and content in the different polymorphs are analogous, as well as the size of crystallites as deduced from the similarity of  $T_m$  values. Thus, the greater  $MH$  found in the HMP $\times$ GLS family compared with that exhibited in the HMP $\times$ GHS set should be ascribed to inherent variations between the two graphene nanofibers and the changes that they imposed within the amorphous PP chains where they are embedded. In fact, the location of glass transition (see results in Table 2), which is a characteristic of the amorphous phase, is found in the HMP $\times$ GLS nanocomposites at higher temperatures than in the HMP $\times$ GHS ones at a similar nanofiber content. The two main differences between these nanofibers are, as aforementioned: their specific surface and the number of graphene layers. As discussed in the morphological features, the former seems to maximize the formation of aggregates in the GHS nanofibers in spite of the number of graphene layers in an individual nanofiber being smaller than in the GLS ones. Thus, the actual GLS domains might be of smaller size and, since dispersion within the iPP matrix is rather uniform in the two sets, lead to higher hindrance in the mobility of the iPP amorphous regions implying higher values of  $T_g$  at a given nanofiber content. These larger motion restrictions involve an increase in stiffness and, then, a rise in  $MH$ .

Results for various mechanical parameters, deduced from the stress-strain curves depicted in Figure 8, are listed in Table 3 for all of the GHS and GLS nanocomposites. The stress-strain curve in the neat HMP is characteristic of a cold drawing behavior. This is a common feature in metallocene iPP [11,23,24]. The S samples become more rigid and brittle than the Q specimens and, accordingly Young's modulus ( $E$ ) and yield stress ( $\sigma_Y$ ) values increase while deformation at break,  $\varepsilon_B$ , is reduced in nanocomposites where a slow

crystallization has been imposed due to its higher  $f_c$  and size of  $\alpha$  crystallites (Q samples do not develop  $\gamma$  crystals). The incorporation of nanofibers adds the presence of another stiff component, independently of the thermal treatment applied in the films, leading to a further increase in parameters related to the rigidity ( $E$  and  $\sigma_Y$ ) and to a reduction in  $\epsilon_B$ . In fact, specimens HMP10GHS and HMP10GLS do not show the yielding point at any thermal treatment.

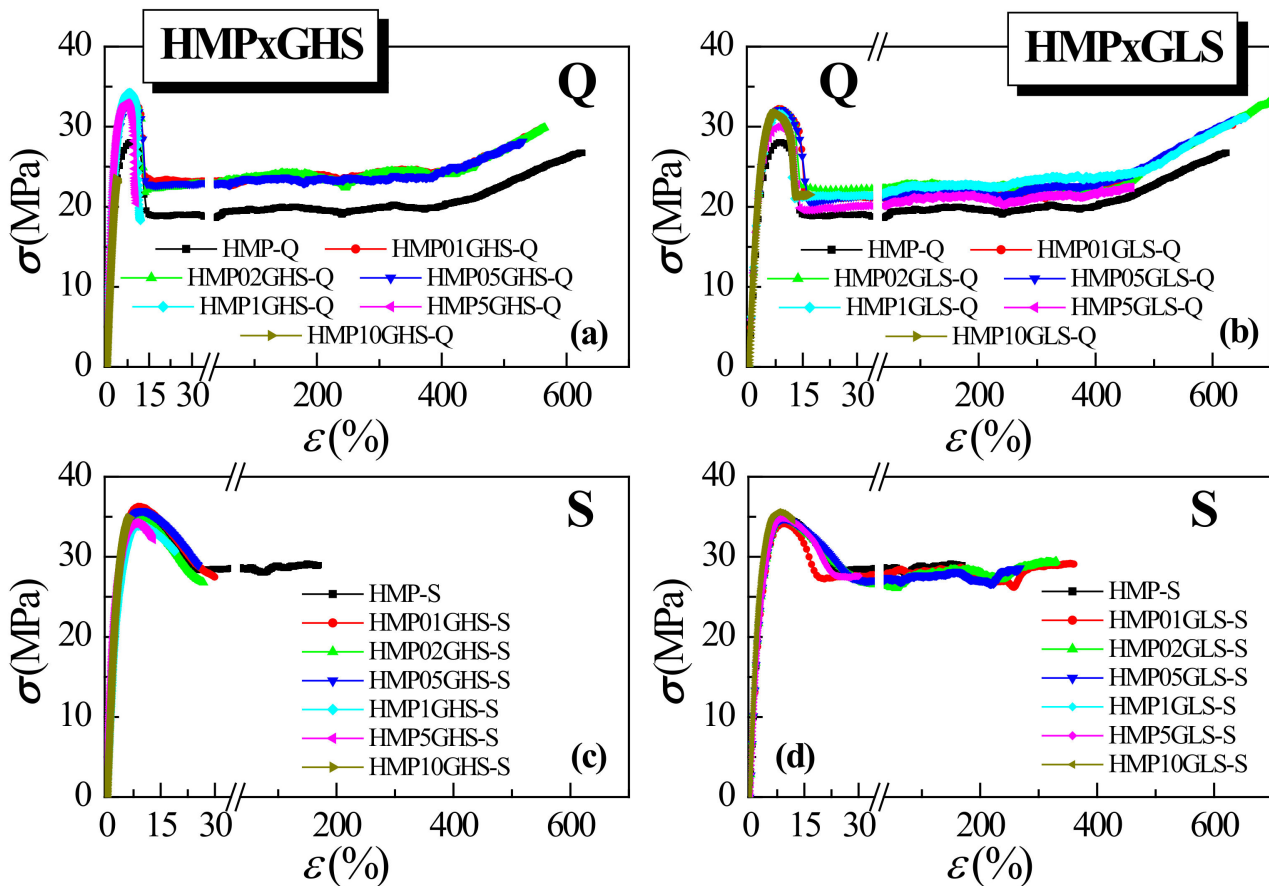


**Figure 8.** Stress-strain curves for the metallocene iPP matrix and nanocomposites with different contents and types of graphene nanofibers: (a) HMPxGHS family with Q treatment; (b) HMPxGLS family with Q treatment; (c) HMPxGHS family with S treatment; and (d) HMPxGLS family with S treatment.

$E$  values (similarly to  $MH$ ) continuously rise with increasing nanofiber content in these nanocomposites, this behavior being slightly different from that described for other graphene composites reported in the literature [24,39–41,56]. Achaby [39] found that  $E$  and tensile strength increased until a 3 wt.% loading in PP/GNs nanocomposites, but elongation at break decreased at these low loadings. Similar results were observed by An [56], so that breaking strength and  $E$  in PP/EG nanocomposite increased significantly with the addition of graphene platelets while breaking strain values decreased. Moreover,  $E$  showed a linear increase with graphene content in the interval analyzed. Bian [40] described much more effective strengthening and toughening effects in a PP matrix with GO functionalized with  $\text{SiO}_2$  than in PP with neat GO. Therefore, an increase of  $E$  was observed in the former nanocomposites compared with that parameter found in the latest. González [24] also reported a reinforcing effect of GNS on a PP matrix. Ryu [41] showed an improvement in the mechanical properties in PP materials with either pristine GO or modified GO with amines, showing these latest formulations a better mechanical performance. Song [38] also observed that the incorporation of graphene nanosheets in a PP matrix led to a significant enhancement of the mechanical strength and  $E$  at low graphene loading while

they diminished gradually at loadings above 2.0 wt.%. Furthermore, elongation at break was significantly reduced with increasing graphene loading level.

**Table 3.** Mechanical parameters for all of the GHS and GLS nanocomposites at the two thermal treatments: Young’s modulus ( $E$ ); yield stress ( $\sigma_Y$ ), yield strain ( $\epsilon_Y$ ); tensile strength ( $\sigma_B$ ), strain at break ( $\epsilon_B$ ).

Sample	E (MPa)	$\sigma_Y$ (MPa)	$\epsilon_Y$ (%)	$\sigma_B$ (MPa)	$\epsilon_B$ (%)
Thermal treatment Q					
HMP-Q	775 ± 30	30.0 ± 1.5	10.0 ± 0.5	31.0 ± 4.5	670 ± 50
HMP01GHS-Q	890 ± 20	30.5 ± 1.5	6.5 ± 0.5	28.0 ± 2.5	560 ± 50
HMP02GHS-Q	900 ± 25	31.0 ± 2.0	7.5 ± 0.5	28.5 ± 3.0	565 ± 50
HMP05GHS-Q	910 ± 40	31.5 ± 1.5	7.0 ± 2.0	25.0 ± 7.0	530 ± 50
HMP1GHS-Q	920 ± 29	32.0 ± 1.5	7.0 ± 0.5	29.0 ± 2.0	8 ± 1
HMP5GHS-Q	940 ± 23	33.0 ± 0.5	6.5 ± 0.1	31.0 ± 0.5	9 ± 1
HMP10GHS-Q	950 ± 10	a	a	16.0 ± 1.5	5 ± 1
HMP01GLS-Q	950 ± 15	31.0 ± 1.0	8.0 ± 0.5	30.0 ± 1.0	640 ± 30
HMP02GLS-Q	960 ± 15	31.5 ± 1.0	7.5 ± 0.5	34.0 ± 2.0	715 ± 30
HMP05GLS-Q	965 ± 10	32.0 ± 1.0	7.0 ± 1.0	34.0 ± 2.0	715 ± 40
HMP1GLS-Q	980 ± 10	32.5 ± 2.0	7.0 ± 1.0	25.5 ± 3.0	610 ± 30
HMP5GLS-Q	995 ± 10	33.0 ± 2.5	6.5 ± 0.5	23.0 ± 1.5	495 ± 25
HMP10GLS-Q	1040 ± 20	a	a	29.0 ± 1.5	9 ± 3
Thermal treatment S					
HMP-S	1000 ± 70	32.3 ± 2.7	8.6 ± 1.0	26.5 ± 1.8	130 ± 40
HMP01GHS-S	1090 ± 30	35.4 ± 0.8	8.2 ± 0.1	26.6 ± 0.6	30 ± 2
HMP02GHS-S	1130 ± 20	35.2 ± 0.3	7.6 ± 0.2	28.7 ± 1.1	25 ± 3
HMP05GHS-S	1140 ± 40	34.3 ± 0.7	7.5 ± 1.1	28.9 ± 0.3	25 ± 5
HMP1GHS-S	1160 ± 20	35.2 ± 0.1	6.2 ± 0.2	32.8 ± 0.1	20 ± 1
HMP5GHS-S	1190 ± 30	33.8 ± 0.4	6.3 ± 0.1	31.3 ± 1.3	18 ± 2
HMP10GHS-S	1250 ± 20	a	a	32.7 ± 0.7	10 ± 1
HMP01GLS-S	1105 ± 17	32.6 ± 3.6	9.2 ± 0.3	27.6 ± 1.3	355 ± 60
HMP02GLS-S	1165 ± 33	35.3 ± 0.2	8.5 ± 0.7	31.2 ± 2.6	325 ± 100
HMP05GLS-S	1195 ± 10	35.4 ± 0.3	7.2 ± 0.4	27.5 ± 1.5	250 ± 20
HMP1GLS-S	1200 ± 20	34.7 ± 0.2	7.3 ± 0.4	26.3 ± 0.7	50 ± 10
HMP5GLS-S	1235 ± 20	34.3 ± 0.6	6.7 ± 0.4	28.5 ± 0.6	25 ± 6
HMP10GLS-S	1315 ± 10	a	a	30.9 ± 1.3	10 ± 1

<sup>a</sup> Yield stress is not reached in most of the specimens stretched since rupture is initiated.

#### 4. Conclusions

Several nanocomposites based on a metallocenic iPP and two types of graphene nanofibers with different specific surfaces (and different number of graphene layers) were prepared by extrusion. Moreover, two thermal treatments were applied during film processing. Their morphological evaluation pointed out a somewhat better homogeneity in the GLS family compared with that observed in the set obtained by incorporation of the GHS nanofibers, because of the highest specific surface in the latest.

There are no significant differences in the crystalline features exhibited by these two sets of nanocomposites in terms of the dependence of the degree of crystallinity, polymorphs developed, or size of crystallites with the type of nanofiber incorporated. Thus, only the monoclinic  $\alpha$  form was observed for all the nanocomposites prepared by rapid crystallization (Q samples), while different proportions of  $\gamma$  orthorhombic and monoclinic  $\alpha$  modifications were achieved for the slowly cooled S samples. Moreover, a higher crystallinity was displayed in the S samples compared with that developed in the Q ones, and also an appreciable increase of crystallinity was noted in the nanocomposites as the graphene content was increased. The presence of nanofibers favors iPP crystallization

by their effect as a nucleating agent, and increasing amounts of the  $\gamma$  form in the S samples were obtained as the nanofiber content increases, in the two types of nanocomposites.

Furthermore, thermal stability in the nanocomposites increased with graphene content, reaching differences in maximum degradation temperature of around 20 °C with respect to that found in the neat polymer.

The most remarkable effect of the type of graphene nanofibers embedded in an iPP matrix was shown in the amorphous regions and in the mechanical response of the nanocomposites. Thus, higher values for microhardness and elastic modulus were attained in the HMP $\alpha$ GLS family compared with those exhibited in the HMP $\alpha$ GHS set. Accordingly, glass transition is located in the HMP $\alpha$ GLS materials at higher temperatures than in the HMP $\alpha$ GHS ones at similar nanofiber content. This fact was attributed to the larger specific surface in the GHS nanofibers that seemed to maximize the formation of aggregates leading to lower motion constraints in the PP amorphous phase of the nanocomposites where they were incorporated. Thus, the smaller GLS domains were able to trigger a large hindrance in the PP mobility, provoking an increase of stiffness and, consequently, higher values in microhardness and Young's modulus.

As a final remark related to environmental concerns, it should be noted that the iPP is fully recyclable. On the other hand, the incorporation of low contents in graphene nanofibers, up to 1% by weight, provides an excellent balance between improvement of rigidity and maintenance of deformation capacity of the iPP matrix. Therefore, it is not expected to negatively influence the recyclability of iPP. This fact makes it possible to maintain the commitment to the environment through its mechanical recycling. Furthermore, at these low contents, the experimental conditions for chemical recycling are not expected to be greatly affected, although studies in this field are not that advanced.

**Author Contributions:** Conceptualization, C.F. and R.B.; methodology, S.N., C.F., R.B., E.B.-B., E.P. and M.L.C.; software, E.P.; validation, S.N., C.F., R.B. and E.B.-B.; formal analysis, S.N., R.B., E.B.-B. and E.P.; investigation, S.N., C.F., R.B., E.B.-B., E.P. and M.L.C.; resources, E.P. and M.L.C.; writing—original draft preparation, S.N., C.F., R.B. and E.P.; writing—review and editing, S.N., C.F., R.B., E.B.-B., E.P. and M.L.C.; supervision, M.L.C.; project administration, E.P. and M.L.C.; funding acquisition, E.P. and M.L.C. All authors have read and agreed to the published version of the manuscript.

**Funding:** This work was supported by the Agencia Estatal de Investigación (AEI, Spain) (grant number PID2020-114930GB-I00).

**Institutional Review Board Statement:** Not applicable.

**Informed Consent Statement:** Not applicable.

**Data Availability Statement:** Not applicable.

**Acknowledgments:** Authors are grateful to the Characterization Service at ICTP-CSIC for SEM, TGA, Raman and mechanical facilities as well as to its personnel for support.

**Conflicts of Interest:** The authors declare no conflict of interest. The funders had no role in the design of the study; in the collection, analyses, or interpretation of data; in the writing of the manuscript, or in the decision to publish the results.

## References

1. Malpass, D.B.; Band, E.I. *Introduction to Industrial Polypropylene: Properties, Catalysts, Processes*; John Wiley & Sons, Inc.: Hoboken, NJ, USA; Scrivener Publishing LLC.: Salem, MA, USA, 2012.
2. Caveda, S.; Pérez, E.; Blázquez-Blázquez, E.; Peña, B.; van Grieken, R.; Suárez, I.; Benavente, R. Influence of structure on the properties of polypropylene copolymers and terpolymers. *Polym. Test.* **2017**, *62*, 23–32. [[CrossRef](#)]
3. Sinn, H.; Kaminisky, W. Ziegler-Natta Catalysis. *Adv. Organomet. Chem.* **1980**, *18*, 99–149.
4. Wild, F.R.W.P.; Zsolnai, L.; Huttner, G.; Brintzinger, H.H. *ansa-Metallocene derivatives IV. Synthesis and molecular structures of chiral ansa-titanocene derivatives with bridged tetrahydroindenyl ligands.* *J. Organomet. Chem.* **1982**, *232*, 233–247. [[CrossRef](#)]
5. Arranz Andrés, J.; Benavente, R.; Peña, B.; Pérez, E.; Cerrada, M.L. Toughening of a propylene-*b*-(ethylene-co-propylene) copolymer by a plastomer. *J. Polym. Sci. Part B Polym. Phys.* **2002**, *40*, 1869–1880. [[CrossRef](#)]



6. Cerrada, M.L.; Benavente, R.; Pérez, E. Crystalline structure and viscoelastic behavior in composites of a metallocenic ethylene-1-octene copolymer and glass fiber. *Macromol. Chem. Phys.* **2002**, *203*, 718–726. [[CrossRef](#)]
7. Prieto, O.; Pereña, J.M.; Benavente, R.; Pérez, E.; Cerrada, M.L. Viscoelastic relaxation mechanisms of conventional polypropylene toughened by a plastomer. *J. Polym. Sci. Part B Polym. Phys.* **2003**, *41*, 1878–1888. [[CrossRef](#)]
8. Krache, R.; Benavente, R.; López-Majada, J.M.; Pereña, J.M.; Cerrada, M.L.; Pérez, E. Competition between  $\alpha$ ,  $\beta$  and  $\gamma$  polymorphs in a  $\beta$ -nucleated metallocenic isotactic polypropylene. *Macromolecules* **2007**, *40*, 6871–6878. [[CrossRef](#)]
9. Benavente, R.; Caveda, S.; Pérez, E.; Blázquez, E.; Peña, B.; van Grieken, R.; Suarez, I. Influence of  $\beta$ -nucleation on polymorphism and properties in random copolymers and terpolymers of propylene. *Polym. Eng. Sci.* **2012**, *52*, 2285–2295. [[CrossRef](#)]
10. Bento, A.; Lourenço, J.P.; Fernandes, A.; Ribeiro, M.R.; Arranz-Andrés, J.; Lorenzo, V.; Cerrada, M.L. Gas permeability properties of decorated MCM 41/polyethylene hybrids prepared by in situ polymerization. *J. Membr. Sci.* **2012**, *415–416*, 702–711. [[CrossRef](#)]
11. Barranco-García, R.; López-Majada, J.M.; Lorenzo, V.; Gómez-Elvira, J.M.; Pérez, E.; Cerrada, M.L. Confinement of iPP chains in the interior of SBA-15 mesostructure ascertained by gas transport properties in iPP-SBA-15 nanocomposites prepared by extrusion. *J. Membr. Sci.* **2019**, *569*, 137–148. [[CrossRef](#)]
12. Kubacka, A.; Cerrada, M.L.; Serrano, C.; Fernández-García, M.; Ferrer, M.; Fernández-García, M. Light-driven novel properties of TiO<sub>2</sub>-modified Polypropylene-based Nanocomposite Films. *J. Nanosci. Nanotechnol.* **2008**, *8*, 3241–3246. [[CrossRef](#)]
13. Blázquez-Blázquez, E.; Arranz-Andrés, J.; Ressia, J.; Vallés, E.M.; Marín, P.; Aragón, A.M.; Pérez, E.; Cerrada, M.L. Electromagnetic Interference Shielding Response and Rheological Behavior of Lightweight Nanocomposites based on isotactic Polypropylene and Al Nanoparticles. *Polym. Test.* **2018**, *72*, 263–270. [[CrossRef](#)]
14. Barranco-García, R.; Gómez-Elvira, J.M.; Ressia, J.A.; Quinzani, L.; Vallés, E.M.; Pérez, E.; Cerrada, M.L. Effect of iPP molecular weight on its confinement within mesoporous SBA-15 silica in extruded iPP-SBA-15 nanocomposites. *Micropor. Mesopor. Mat.* **2020**, *294*, 109945. [[CrossRef](#)]
15. Barranco-García, R.; Gómez-Elvira, J.M.; Ressia, J.A.; Quinzani, L.; Vallés, E.M.; Pérez, E.; Cerrada, M.L. Variation of Ultimate Properties in Extruded iPP-Mesoporous Silica Nanocomposites by Effect of iPP Confinement within the Mesostructures. *Polymers* **2020**, *12*, 70. [[CrossRef](#)]
16. Palza, H.; López-Majada, J.M.; Quijada, R.; Pereña, J.M.; Benavente, R.; Pérez, E.; Cerrada, M.L. Comonomer Length Influence on the Structure and Mechanical Response of Metallocenic Polypropylenic Materials. *Macromol. Chem. Phys.* **2008**, *209*, 2259–2267. [[CrossRef](#)]
17. Barranco-García, R.; Ferreira, A.E.; Ribeiro, M.R.; Lorenzo, V.; García-Peñas, A.; Gómez-Elvira, J.M.; Pérez, E.; Cerrada, M.L. Hybrid materials obtained by in situ polymerization based on polypropylene and mesoporous SBA-15 silica particles: Catalytic aspects, crystalline details and mechanical behavior. *Polymer* **2018**, *151*, 218–230. [[CrossRef](#)]
18. Ahmad, S.R.; Young, R.J.; Kinloch, I.A. Raman spectra and mechanical properties of graphene/polypropylene nanocomposites. *Int. J. Chem. Eng. Appl.* **2015**, *6*, 1–5.
19. Yang, K.; Endoh, M.; Trojanowski, R.; Ramasamy, R.P.; Gentlman, M.M.; Butcher, T.A.; Rafailovich, M.H. The thermo-mechanical response of PP nanocomposites at high graphene loading. *Nanocomposites* **2015**, *1*, 126–137. [[CrossRef](#)]
20. Al-Saleh, M.A.; Yussuf, A.A.; Al-Enezi, S.; Kazemi, R.; Wahit, M.U.; Al-Shammari, T.; Al-Banna, A. Polypropylene/Graphene Nanocomposites: Effects of GNP Loading and Compatibilizers on the Mechanical and Thermal Properties. *Materials* **2019**, *12*, 3924. [[CrossRef](#)]
21. Milani, M.A.; Quijada, R.; Basso, N.R.S.; Graebin, A.P.; Galland, G.B. Influence of the graphite type on the synthesis of polypropylene/graphene nanocomposites. *J. Polym. Sci. Part A Polym. Chem.* **2012**, *50*, 3598–3605. [[CrossRef](#)]
22. Milani, M.A.; González, D.; Quijada, R.; Basso, N.R.S.; Cerrada, M.L.; Azambuja, D.S.; Galland, G.B. Polypropylene/graphene nanosheet nanocomposites by in situ polymerization: Synthesis, characterization and fundamental properties. *Compos. Sci. Technol.* **2013**, *84*, 1–7. [[CrossRef](#)]
23. Milani, M.A.; González, D.; Quijada, R.; Benavente, R.; Arranz-Andrés, J.; Galland, G.B. Synthesis, characterization and properties of poly(propylene-1-octene)/graphite nanosheet nanocomposites obtained by in situ polymerization. *Polymer* **2015**, *65*, 134–142. [[CrossRef](#)]
24. González, D.M.; Quijada, R.; Yazdani-Pedram, M.; Benavente, R.; Galland, G.B.; Milani, M.A. Influence of the Polymeric Matrix and Thermal Treatment on the Properties of Polyolefin-Graphite Nanosheets Nanocomposites. *Macromol. Mater. Eng.* **2016**, *301*, 1503–1512. [[CrossRef](#)]
25. Klug, P.; Alexander, L.E. *X-ray Diffraction Procedures: For Polycrystalline and Amorphous Materials*, 2nd ed.; John Wiley & Sons, Inc.: Hoboken, NJ, USA, 1974.
26. Mansel, S.; Pérez, E.; Benavente, R.; Pereña, J.M.; Bello, A.; Roll, W.; Kirsten, R.; Beck, S.; Brintzinger, H.H. Synthesis and properties of elastomeric poly (propylene). *Macromol. Chem. Phys.* **1999**, *200*, 1292–1297. [[CrossRef](#)]
27. Arranz-Andrés, J.; Parrilla, R.; Cerrada, M.L.; Pérez, E. Mesophase Formation in Random Propylene-co-1-Octene Copolymers. *Macromolecules* **2013**, *46*, 8557–8568. [[CrossRef](#)]
28. Mezghani, K.; Philips, P.J. The  $\gamma$ -phase of high molecular weight isotactic polypropylene: III. The equilibrium melting point and the phase diagram. *Polymer* **1998**, *39*, 3735–3744. [[CrossRef](#)]
29. Bond, E.B.; Spruiell, J.E.; Lin, J.S. A WAXD/SAXS/DSC study on the melting behavior of Ziegler-Natta and metallocene catalyzed isotactic polypropylene. *J. Polym. Sci. Part B Polym. Phys.* **1999**, *37*, 3050–3064. [[CrossRef](#)]
30. Baltá-Calleja, F.J. Microhardness Relating to Crystalline Polymers. *Adv. Polym. Sci.* **1985**, *66*, 117–148.

31. Fonseca, C.; Pereña, J.M.; Benavente, R.; Cerrada, M.L.; Bello, A.; Pérez, E. Microhardness and thermal study of the annealing effects in vinyl alcohol-ethylene copolymers. *Polymer* **1995**, *36*, 1887–1892. [[CrossRef](#)]
32. Pedrazzoli, D.; Dorigato, A.; Conti, T.; Vanzetti, L.; Bersani, M.; Pegoretti, A. Liquid crystalline polymer nanocomposites reinforced with in-situ reduced graphene oxide. *eXPRESS Polym. Lett.* **2015**, *9*, 709–720. [[CrossRef](#)]
33. Ferrari, A.C. Raman spectroscopy of graphene and graphite: Disorder, electron–phonon coupling, doping and nonadiabatic effects. *Solid State Commun.* **2007**, *143*, 47–57. [[CrossRef](#)]
34. Marquina, J.; Power, C.; González, J. Raman spectroscopy in monolayer graphene and graphite: Electron-phonon coupling and nonadiabatic effects. *Tumbaga* **2010**, *5*, 183–194.
35. Monti, M.; Rallini, M.; Puglia, D.; Peponi, L.; Torre, L.; Kenny, J.M. Morphology and electrical properties of graphene–epoxy nanocomposites obtained by different solvent assisted processing methods. *Compos. Part A Appl. Sci. Manuf.* **2013**, *46*, 166–172. [[CrossRef](#)]
36. Bunch, J.S.; Yaish, Y.; Brink, M.; Bolotin, K.; McEuen, P.L. Coulomb Oscillations and Hall Effect in Quasi-2D Graphite Quantum Dots. *Nano Lett.* **2005**, *5*, 287–290. [[CrossRef](#)]
37. Gupta, A.; Chen, G.; Joshi, P.; Tadigadapa, S.; Eklund, P.C. Raman scattering from high-frequency phonons in supported n-graphene layer films. *Nano Lett.* **2006**, *6*, 2667–2673. [[CrossRef](#)]
38. Song, P.; Cao, Z.; Cai, Y.; Zhao, L.; Fang, Z.; Fu, S. Fabrication of exfoliated graphene-based polypropylene nanocomposites with enhanced mechanical and thermal properties. *Polymer* **2011**, *52*, 4001–4010. [[CrossRef](#)]
39. El Achaby, M.; Arrakhiz, F.E.; Vaudreuil, S.; El Kacem Qaiss, A.; Bousmina, M.; Fassi-Fehri, O. Mechanical, thermal, and rheological properties of graphene-based polypropylene nanocomposites prepared by melt mixing. *Polym. Compos.* **2012**, *33*, 733–744. [[CrossRef](#)]
40. Bian, J.; Wang, Z.J.; Lin, H.L.; Zhou, X.; Xiao, W.Q.; Zhao, X.W. Thermal and mechanical properties of polypropylene nanocomposites reinforced with nano-SiO<sub>2</sub> functionalized graphene oxide. *Compos. Part A Appl. Sci. Manuf.* **2017**, *97*, 120–127. [[CrossRef](#)]
41. Ryu, S.H.; Shanmugharaj, A.M. Influence of hexamethylene diamine functionalized graphene oxide on the melt crystallization and properties of polypropylene nanocomposites. *Mater. Chem. Phys.* **2014**, *146*, 478–486. [[CrossRef](#)]
42. Long, J.; Li, S.; Liang, J.; Wang, J.; Liang, B. Preparation and characterization of graphene oxide and its application as a reinforcement in polypropylene composites. *Polym. Compos.* **2019**, *40*, 723–729. [[CrossRef](#)]
43. Turner-Jones, A.; Aizlewood, J.M.; Beckett, D.R. Crystalline forms of isotactic polypropylene. *Makromol. Chem.* **1964**, *75*, 134–158. [[CrossRef](#)]
44. Brückner, S.; Meille, S.V.; Petraccone, V.; Pirozzi, B. Polymorphism in isotactic polypropylene. *Prog. Polym. Sci.* **1991**, *16*, 361–404. [[CrossRef](#)]
45. Varga, J. Supermolecular structure of isotactic polypropylene. *J. Mat. Sci.* **1992**, *27*, 2557–2579. [[CrossRef](#)]
46. Lotz, B.; Wittmann, J.C.; Lovinger, A.J. Structure and morphology of poly(propylenes): A molecular analysis. *Polymer* **1996**, *37*, 4979–4992. [[CrossRef](#)]
47. Polo-Corpa, M.J.; Benavente, R.; Velilla, T.; Quijada, R.; Pérez, E.; Cerrada, M.L. Development of the mesomorphic phase in isotactic propene/higher  $\alpha$ -olefin copolymers at intermediate comonomer content and its effect on properties. *Eur. Polym. J.* **2010**, *46*, 1345–1354. [[CrossRef](#)]
48. Pérez, E.; Gómez-Elvira, J.M.; Benavente, R.; Cerrada, M.L. Tailoring the formation rate of the mesophase in random propylene-co-1-pentene copolymers. *Macromolecules* **2012**, *45*, 6481–6490. [[CrossRef](#)]
49. Poon, B.; Rogunova, M.; Hiltner, A.; Baer, E.; Chum, P.S.; Galeski, A.; Piorkowska, E. Structure and properties of homogeneous copolymers of propylene and 1-hexene. *Macromolecules* **2005**, *38*, 1232–1243. [[CrossRef](#)]
50. De Rosa, C.; Dello Iacono, S.; Auriemma, F.; Ciaccia, E.; Resconi, L. Crystal structure of isotactic propylene-hexene copolymers: The trigonal form of isotactic polypropylene. *Macromolecules* **2006**, *39*, 6098–6109. [[CrossRef](#)]
51. Pérez, E.; Cerrada, M.L.; Benavente, R.; Gómez-Elvira, J.M. Enhancing the formation of the new trigonal polymorph in isotactic propene-1-pentene copolymers: Determination of the X-ray crystallinity. *Macromol. Res.* **2011**, *19*, 1179–1185. [[CrossRef](#)]
52. García-Peñas, A.; Gómez-Elvira, J.M.; Pérez, E.; Cerrada, M.L. Isotactic poly(propylene-co-1-pentene-co-1-hexene) terpolymers: Synthesis, molecular characterization, and evidence of the trigonal polymorph. *J. Polym. Sci. Part A Polym. Chem.* **2013**, *51*, 3251–3259. [[CrossRef](#)]
53. García-Peñas, A.; Gómez-Elvira, J.M.; Barranco-García, R.; Pérez, E.; Cerrada, M.L. Trigonal form as a tool for tuning mechanical behavior in poly(propylene-co-1-pentene-co-1-heptene) terpolymers. *Polymer* **2016**, *99*, 112–121. [[CrossRef](#)]
54. Pérez, E.; Zucchi, D.; Sacchi, M.C.; Forlini, F.; Bello, A. Obtaining the  $\gamma$  phase in isotactic polypropylene: Effect of catalyst system and crystallization conditions. *Polymer* **1999**, *40*, 675–681. [[CrossRef](#)]
55. Ahmad, S.R.; Xue, C.; Young, R.J. The mechanisms of reinforcement of polypropylene by graphene nanoplatelets. *Mater. Sci. Eng. B* **2017**, *216*, 2–9. [[CrossRef](#)]
56. An, J.E.; Jeon, G.W.; Jeong, Y.G. Preparation and properties of polypropylene nanocomposites reinforced with exfoliated graphene. *Fibers Polym.* **2012**, *13*, 507–514. [[CrossRef](#)]
57. Wang, Y.; Wang, J.-C.; Chen, S.-Z. Role of surfactant molecular weight on morphology and properties of functionalized graphite oxide filled polypropylene nanocomposites. *eXPRESS Polym. Lett.* **2014**, *8*, 881–894. [[CrossRef](#)]

58. Campos, J.M.; Lourenço, J.P.; Pérez, E.; Cerrada, M.L.; Ribeiro, M.R. Self-Reinforced Hybrid Polyethylene/MCM-41 Nanocomposites: In-Situ Polymerisation and Effect of MCM-41 Content on Rigidity. *J. Nanosci. Nanotechnol.* **2009**, *9*, 3966–3974. [[CrossRef](#)] [[PubMed](#)]
59. Cerrada, M.L.; de la Fuente, J.L.; Fernández-García, M.; Madruga, E.L. Viscoelastic and mechanical properties of poly(butyl acrylate-g-styrene) copolymers. *Polymer* **2001**, *42*, 4647–4655. [[CrossRef](#)]